Supporting information

Sustainable Sulfur-Carbonaceous Composite Electrode Toward High Specific Energy Rechargeable Cells

Yoon Hwa,[1,2,‡] Hyo Won Kim,[1,2,3‡] Hao Shen,[3,4] Dilworth Y. Parkinson,[3] Bryan D. McCloskey,[1,2] and Elton J. Cairns[1,2,*]

[1] Energy Storage and Distributed Resources Division, Lawrence Berkeley National Laboratory, One Cyclotron Rd., Berkeley, California, 94720, USA

[2] Department of Chemical and Biomolecular Engineering, University of California, Berkeley, California, 94720, USA

[3] Department of Advanced Materials Engineering, Kangwon National University, Samcheok 25931, Republic of Korea

[4] Advanced Light Source, Lawrence Berkeley National Laboratory, One Cyclotron Rd., Berkeley, California, 94720, USA

[5] Center for Advancing Materials Performance from the Nanoscale (CAMP-Nano), State Key Laboratory for Mechanical Behavior of Materials, Xi'an Jiaotong University, Xi'an, Shaanxi 710049, China

Corresponding Author

*Elton J. Cairns (ejcairns@lbl.gov)

EXPERIMENTAL METHODS

1. Materials: Fine grade synthetic graphite powder (SP-1) was purchased from Bay Carbon Inc. (Bay city, MI, USA) and used as received. Sulphuric acid (H_2SO_4, 97%), hydrochloric acid (HCl, 35% in water) and acetone (CH_3COCH_3, 99.5%) from Daejung Chemicals & Metals Co. (Siheung, Korea); Hydrogen peroxide (H_2O_2, 50% in water), phosphorous pentoxide (P_2O_5, 98%), ethylenediaminetetraacetic acid (EDTA, ACS reagent), urea (ACS reagent), hydrazine monohydrate ($N_2H_4 \cdot H_2O$, 64-65%, reagent grade 98%), ammonium hydroxide solution (NH_4OH, 28.0-30.0 %, ACS reagent), dioxolane (DOL, 99.8%), dimethoxyethane (DME, 99.9%), styrene-butadiene rubber (SBR) and carboxymethyl cellulose (CMC) and bis(trifluoromethanesulfonyl)imide lithium salt (LiTFSI) from Aldrich Chemical Co.; Lithium nitrate ($LiNO_3$, Anhydrous, 99.999%), N-methyl-2-pyrrolidone (NMP, 99+%), sodium sulfide (Na_2S, anhydrous) and sulfur (S, ~325 mesh, 99.5%) from Alfa Aesar were used. Potassium permanganate ($KMnO_4$, JUNSEI Chemical Co.), lithium metal (Li, FMC), N-methyl N-butylpyrrolidinium bis(trifluoromethanesulfonyl)imide ($PYR_{14}TFSI$, Coorstek), formic acid (CH_3COOH, Aqua Solutions), Super P (Timcal) and carbon nanotubes (CNT, OCSiAl) were also used as received.

2. Synthesis of *N*rGO*:* GO was synthesized using the modified Hummers method. The *N*rGO was prepared by a mild thermal reduction.[1] Briefly, GO (0.1 wt.%) was dispersed in water into a three-neck round-bottle flask by stirring for 30 min and sonication for 90 min with sonication power and frequency of 100 W and 40 KHz, respectively. After that, we performed simultaneous nitrogen doping and mild reduction of a well-dispersed GO (0.1 wt.%) in water by adding NH_4OH solution (0.01 wt.%) as a nitrogen source at 80.0 or 100.0 ^oC under N_2 purge. After 15 hours, the product was carefully filtered and rinsed several times with ultra-purified water to

avoid unwanted gelation or aggregation, and the dispersed material was kept in water before using.

3. Synthesis of S-*N*rGO composite*:* The S-*Nr*GO composite was prepared as follows. Briefly, 0.406 g of Na_2S powder was dissolved in 17.5 mL of ultrapure water and then 0.504 g of S powder was added to the Na_2S solution and stirred with a magnetic stirrer until the solution became a transparent orange-colored Na_2S_x solution. The prepared Na_2S_x solution was added to 180 ml of the prepared *N*rGO suspension in water (0.5 mg/ml) and stirred overnight. The as-prepared Na_2S_x-*N*rGO composite solution was slowly added to 100 mL of 2.0 M formic acid and stirred for two hours. To remove salts and impurities from the S-*N*rGO suspension, the supernatant was discarded followed by adding ultrapure water, repeatedly, until the pH of the suspension reached about 7.0. Finally, the S-*N*rGO composite in approximately 100.0 mL of water was frozen at −85.0 °C and lyophilized (Labconco) at 15.0 moor. For the aggregated S-*N*rGO composite, the S-*N*rGO suspension was filtered and washed with ultrapure water several times to remove salts and impurities. The obtained powder sample was dried at 50.0 °C in a vacuum oven overnight. Both the S-*N*rGO and the aggregated S-*N*rGO were heat-treated in a tube furnace at 155 °C for 18 h under an Ar atmosphere.

4. Material characterization*:* X-ray photoelectron spectroscopy (XPS) was performed using a monochromatized Al Kα X-ray source (Quantum2000, Physical Electronics, Chanhassen, MN, USA). XPS used at 4 nm slot was conducted under extremely high vacuum at 10-9 torr, and the average acquisition times are at about 30 min for each procedure. C1s peak data were collected to analyze the chemical structure of the *N*rGO. The surface area was calculated by the Brunauer-Emmett-Teller (BET) method. Nitrogen (N_2) gas adsorption isotherms were measured at 77.0 K by using a surface area and porosimetry analyzer (ASAP 2020, Micromeritics Instrument Corp.,

Norcross, GA, USA). Samples were placed in the sample chamber and exposed to vacuum overnight at 60 ^{o}C to remove other gas impurities, and the dried sample weight was measured to calculate the specific area corresponding to the adsorbed amount of N_2. BJH adsorption method with the Kelvin model of pore filling was used for pore size distribution analysis. Scanning helium ion microscopy (HIM, Zeiss ORION NanoFab) was carried out to observe the detailed structural morphology of the S-*N*rGO, aggregated S-*N*rGO and S-*N*rGO-100 composites. No sample damage was found during the observation. The morphology of the pristine and the cycled S-*N*rGO and S-*N*rGO-100 electrodes were observed using a scanning electron microscope (SEM, ZEISS Gemini Ultra 55). Thermogravimetric analysis (TGA, TA Instruments Q5000) was used to determine the content of S in the S-*N*rGO composites up to 600 °C under a Ar atmosphere with a temperature ramping rate of 5.0 ^{o}C/min and a gas flow rate of 60 ml/min. The contents of carbon, nitrogen and oxygen in the prepared *N*rGO and the *N*rGO-100 were determined by elemental analysis (Perkin Elmer 2400 Series Ⅱ Combustion Analyzer). A Bruker Avance 500 MHz spectrometer was used to measure the solid-state ^{13}C CP/MAS NMR at 10 kHz spinning speed. Each spectrum for direct ^{13}C observation with ^{1}H decoupling was conducted 2560 scans. 1024 scans with 100 micron second time were employed for cross polarization measurements.

5. Polysulfide dissolution/adsorption test*:* For the polysulfide dissolution test of the S-*N*rGO and the aggregated S-*N*rGO composites 1 mg of the powder was put into a test solution composed of 1 M LiTFSI in 2 mL of DOL/DME mixture (1:1, *v/v*) with 1.1 mg of Li_2S powder added. For the polysulfide absorption test of the *N*rGO, 1 mg of the *N*rGO powder was put into a test solution composed of 0.008 M Li_2S_8 in 2 mL of DOL/DME mixture (1:1, *v/v*) overnight.

6. Micro X-ray computed tomography (micro X-ray CT)*:* The synchrotron micro X-ray CT experiment is performed on Beamline 8.3.2 in Advanced Light Source (ALS). All electrodes are

casted on the Al foils and powder samples were put into Kapton tubes, and scanned by the 24 keV monochromatic X-ray beam. The resolution is around 1 μm. Then the raw data was analyzed by ImageJ and the 3D model was reconstructed by using the software Avizo.

7. Electrochemical tests: The S-*N*rGO electrodes (≤3 mgS cm^{-2}) were prepared by mixing the S-*N*rGO composite and Super P with a binder (SBR:CMC=1:1, *w/w*) at a weight ratio of 64:28:8 in ultrapure water. The slurries were stirred using a magnetic stirrer overnight and cast *via* a doctor blade onto an aluminum foil. For the high sulfur loading S-*N*rGO electrodes (> 6 mgS/cm^2), the slurry formula was modified as follows: S-*N*rGO composite:Super P:CNT:SBR/CMC = 74.1:17.5:0.4:8.0. The weight ratio between SBR and CMC is 1:1. The electrodes were dried at room temperature for 6.0 h, and then dried in a vacuum oven at 50.0 °C overnight to fully eliminate residual water. Two different electrolytes composed of 1.0 M LiTFSI and 0.21 M $LiNO_3$ in PYR_{14}TFSI/DOL/DME (2:1:1, *v/v/v*) and 1.0 M LiTFSI and 0.5 M $LiNO_3$ in DOL/DME (1:1, v/v) were used for the low S mass loading electrodes and the high mass loading electrodes, respectively. Addition of ionic liquid in the electrolyte helps to improve cell cycle life and Coulombic efficiency because low polysulfide solubility and high viscosity of ionic liquid suppresses polysulfide shuttle effect.[1,2] Coin cells (2032-type) were fabricated with a Li metal foil as counter/reference electrode and a porous polypropylene separator (Celgard 2400) in a glovebox filled with Ar gas. The amount of the electrolyte was adjusted depending on the S mass loading of the S electrode to achieve the desired E/S ratio. Galvanostatic cycling tests of the coin cells were performed using a battery cycler (Maccor) at a given current density. The electrochemical impedance was measured from 10 mHz to 1 MHz using a potentiostat (Biologic VSP) at the charged state. For ex-situ UV-Vis tests, the cells were collected at the fully discharged state (1.7 V) or the charged state (2.7 V) and disassembled immediately. Then, all

cell components that contain electrolyte (cathode can, S electrode, spacer, separator, Li electrode) were put into the DOL/DME mixture (1:1, *v/v*) to collect all of the electrolyte from the cycled cell. The collected electrolyte solution was tested by UV-Vis spectroscopy. For the catholyte cell test, the *N*rGO electrodes were prepared by mixing the *N*rGO (or the aggregated *N*rGO) and PVDF as a binder at a weight ratio of 70:30 in NMP. The electrolyte was composed of DOL:DME (1:1, *v/v*) with 1 M LITFSI and 0.008 M Li_2S_8.

Supplementary Figures

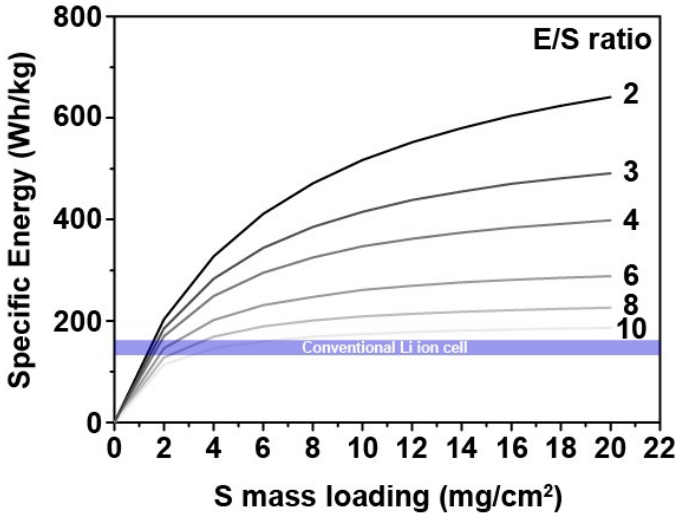

Fig. S1 Specific energy design calculation for Li/S pouch cells.

The specific energy of pouch cells was estimated under the assumptions: specific capacity of 1000 mAh/gS; Nominal cell voltage of 2.15 V, two times larger stoichiometric amount of lithium required for 1000 mAh/gS; aluminum (thickness: 17 um) and copper foil current collectors (thickness: 15 um) for sulfur and lithium electrodes, respectively; the weight of pouch, Ni and Al tabs and separator are included; electrode area of 84.0 cm^2; six sulfur laminates.

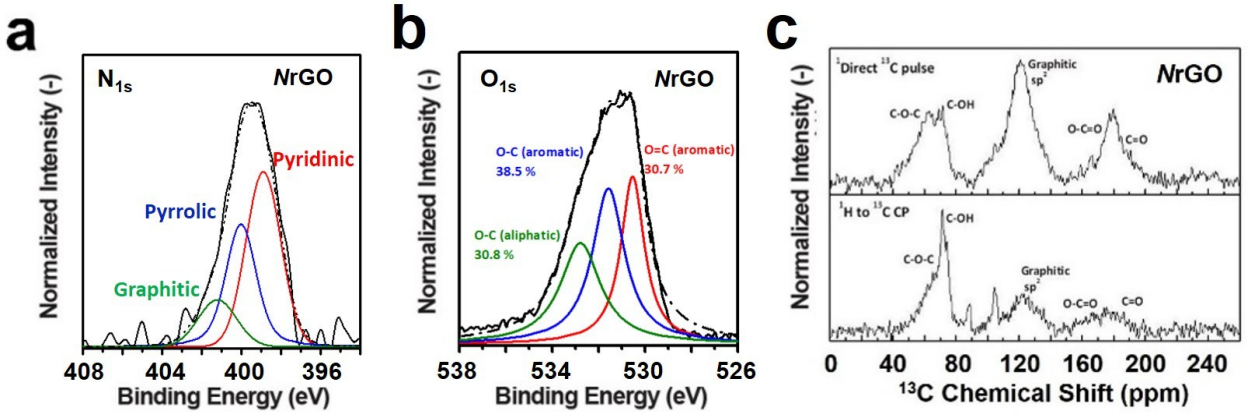

Fig. S2 (a) N_{1s} and (b) O_{1s} XPS spectra of the *N*rGO. (c) Solid-state ^{13}C CP/MAS NMR spectra of the *N*rGO.

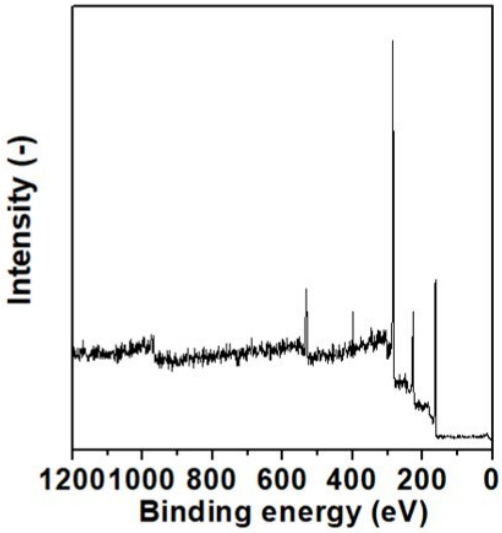

Fig. S3 XPS survey scan of the S-*N*rGO composite.

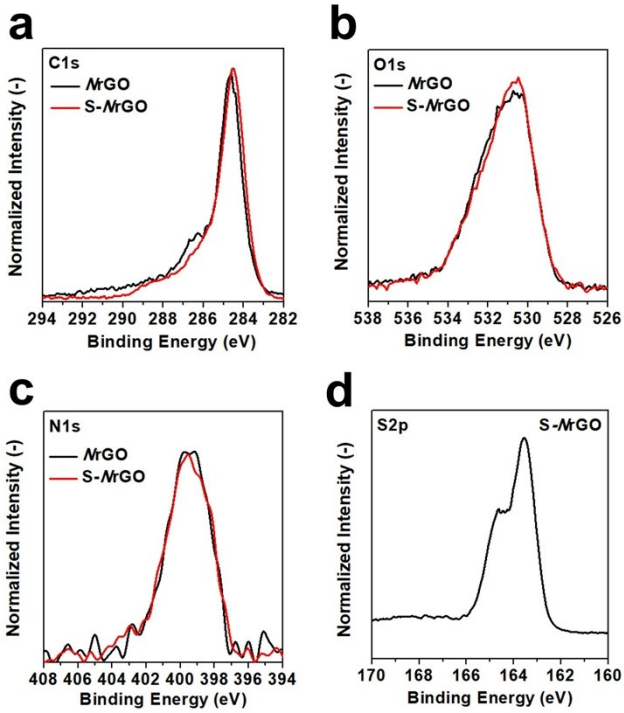

Fig. S4 XPS results of the *N*rGO and the S-*N*rGO composite. (a) C_{1s}, (b) O_{1s} and (c) N_{1s} XPS spectra. (d) S_{2p} XPS spectra of the S-*N*rGO composite.

As shown in Fig. S4a-S4c, XPS spectra of the as-prepared *N*rGO and the *N*rGO in the S-*N*rGO composite are almost same, which means that the chemical structure of the *N*rGO was maintained after S deposition process. The S_{2P} XPS spectra of the S-*N*rGO composite (Fig. S4d) indicates existence of elemental sulfur in the S-*N*rGO composite.

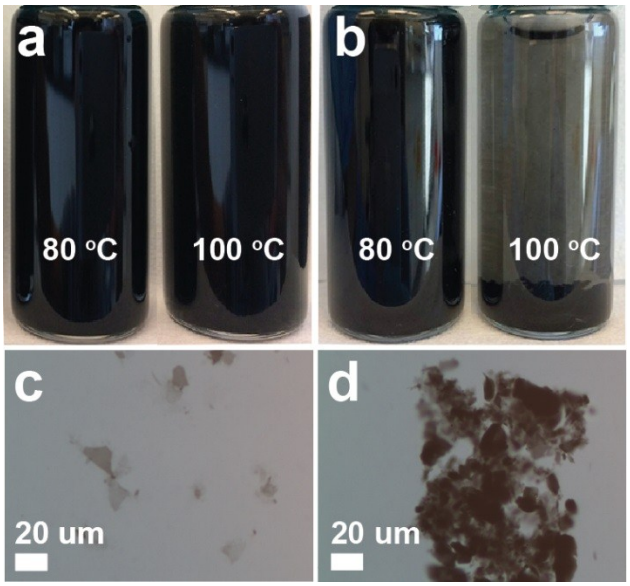

Fig. S5 Photo of the *N*rGO suspensions. (a) Just sonicated and (b) after two days. Optical microscope images of the *N*rGO suspensions prepared at (c) 80.0 °C and (d) 100.0 °C.

As shown in Fig. S5a and S5b, the *N*rGO suspension prepared at 80.0 °C is very stable, whereas the *N*rGO flakes prepared at 100 °C obviously settled after two days. Very thin and individual *N*rGO flakes were easily found in the *N*rGO suspension prepared at 80.0 °C under the optical microscope, which is in contrast to the *N*rGO flakes synthesized at 100.0 °C, where the flakes are severely aggregated.

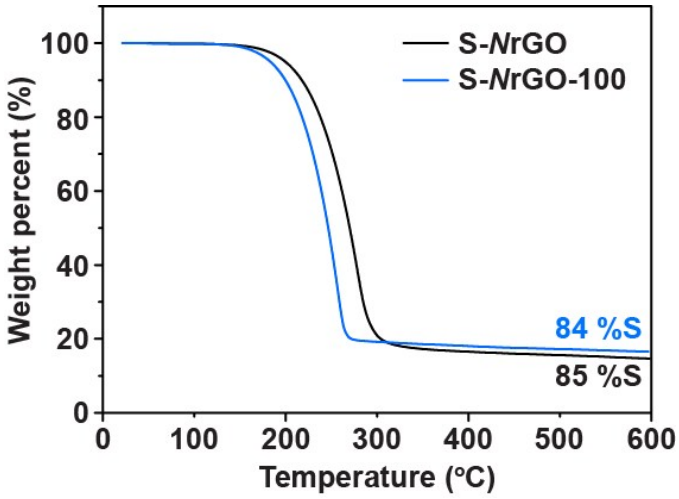

Fig. S6 TGA result of the S-*N*rGO and the S-*N*rGO-100 composites under Ar atmosphere with a temperature ramping rate of 5.0 °C/min.

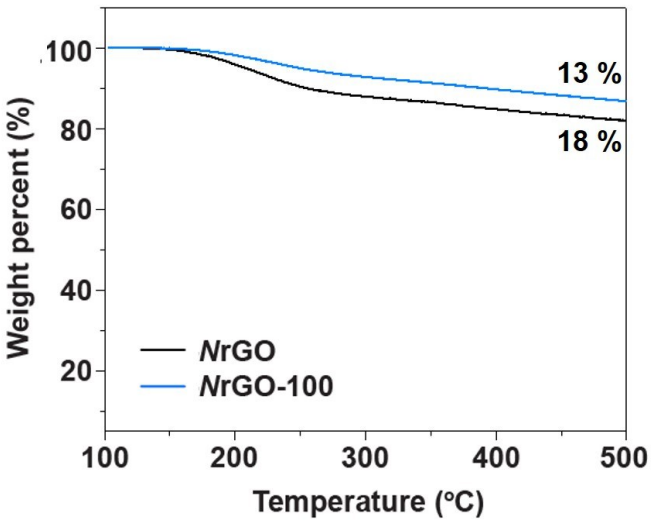

Fig. S7 TGA result of the *N*rGO and the *N*rGO-100 composites under Ar atmosphere with a temperature ramping rate of 5.0 °C/min.

As shown in Fig. S6, 15 wt. % remains after TGA analysis of the S-*N*rGO. Considering that 82 wt. % remains after the TGA analysis of the *N*rGO (Fig. S7), the maximum weight loss contribution of the *N*rGO (x) for the TGA analysis of the S-*N*rGO can be estimated by 15 wt.% : x wt.%= 82 wt.% : 18 wt.%. Thus, 3.3 wt.% loss for the S-*N*rGO composite could be attributed to the *N*rGO, in maximum. Through the same calculation for the S-*N*rGO-100 composite, 2.4 wt.% is obtained. However, it is unlikely these maximum values are fully considered because (1) according to the previous report,[1] partial reduction of GO may occur during the synthesis of the S-GO composite involving Na_2S_x as a source of sulfur; (2) if evolution of CO_2 gas occurs during TGA analysis of the S-*N*rGO and the S-*N*rGO-100 composites in accordance with the amount of oxygen present in the *N*rGO and *N*rGO-100, the S-*N*rGO composite should exhibit more obvious weight loss around 150-200 ℃ than the S-*N*rGO-100 composite during the TGA analysis, since the *N*rGO has higher oxygen content and showed steeper weight decrease than the *N*rGO-100 (Fig. S7), which does not correspond to the TGA results of the S-*N*rGO and S-*N*rGO-100 composite. Consequently, the contribution of the *N*rGO and the *N*rGO-100 to the weight loss of their sulfur composite during the TGA analyses, is less than 3.3 wt.% and 2.4 wt.% respectively.

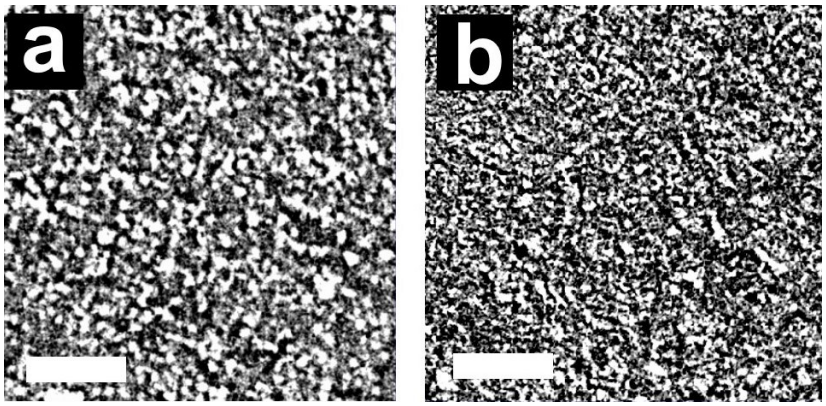

Fig. S8 Gray-scale in-plane cross section of (a) the S-*N*rGO electrode and the S-*N*rGO-100 electrode. (Scale bar: 100 μm, subvolume: 400 μm × 400 μm × 50 μm).

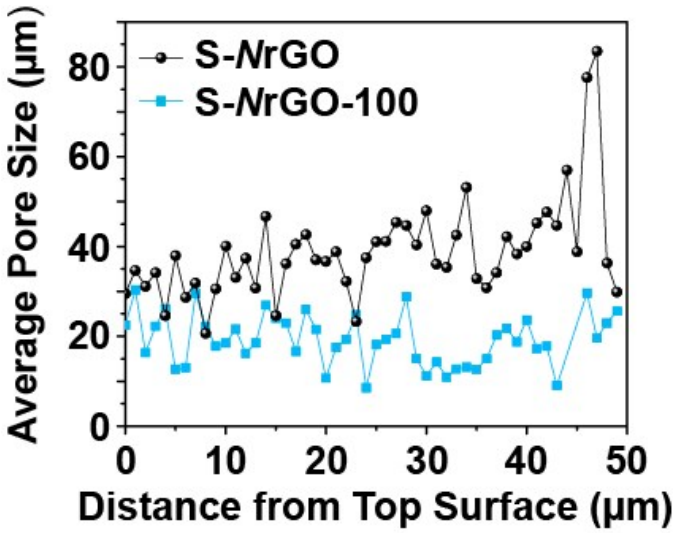

Fig. S9 Porosity estimation results of the S-*N*rGO and the S-*N*rGO-100 electrodes obtained from micro X-ray CT results.

The porosity for the 50 μm thickness range of the electrodes (from top surface to the interior of the electrodes) was evaluated and an average value is taken every 5 frames.

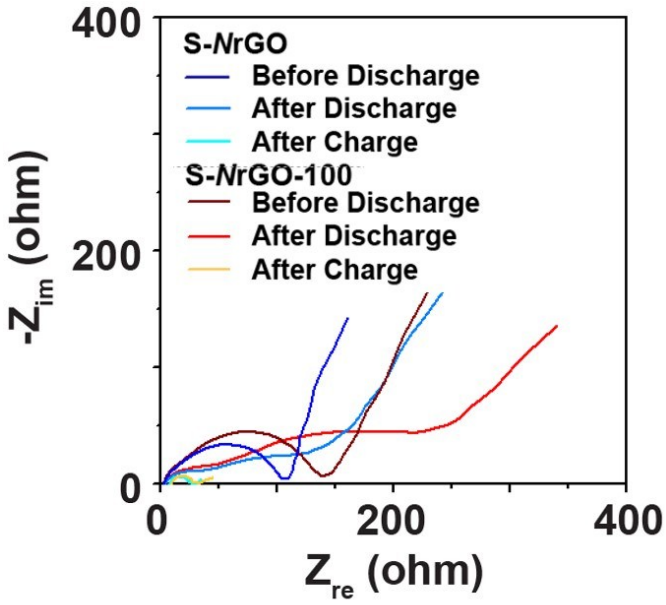

Fig. S10 Electrochemical behavior of the S-*N*rGO and the S-*N*rGO-100 electrodes. Nyquist plots obtained in the frequency range of 10.0 mHz to 1.0 MHz. The electrolyte was composed of 1 M LITFSI and 0.5 M $LiNO_3$ in DOL:DME (1:1, *v/v*). The sulfur mass loading of the electrodes is ~ 7.2 mgS/cm^2. The E/S ratio was 5.

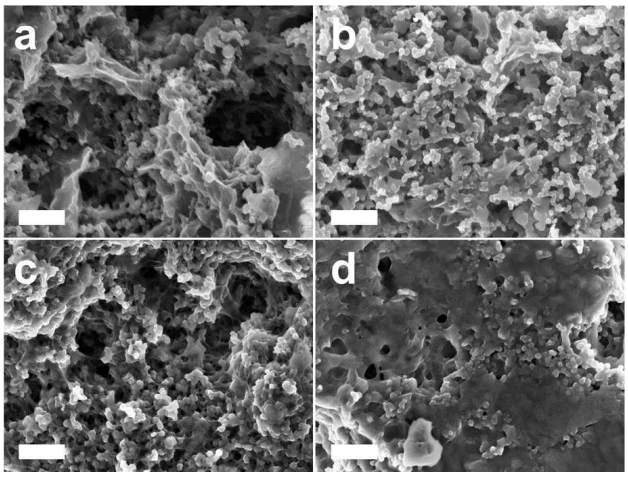

Fig. S11 SEM images of the S-*N*rGO and the S-*N*rGO-100 electrodes. Pristine: (a) S-*N*rGO and (b) S-*N*rGO-100 electrodes. The electrodes after complete discharge and charge processes: (c) the S-*N*rGO and (d) the S-*N*rGO-100 electrode. The electrodes were cycled with an electrolyte composed of 1.0 M LITFSI and 0.5 M $LiNO_3$ in DOL:DME (1:1, *v/v*). Sulfur mass loading of the electrodes is ~ 7.2 mgS/cm^2. E/S ratio was 5. (scale bar: 200 nm)

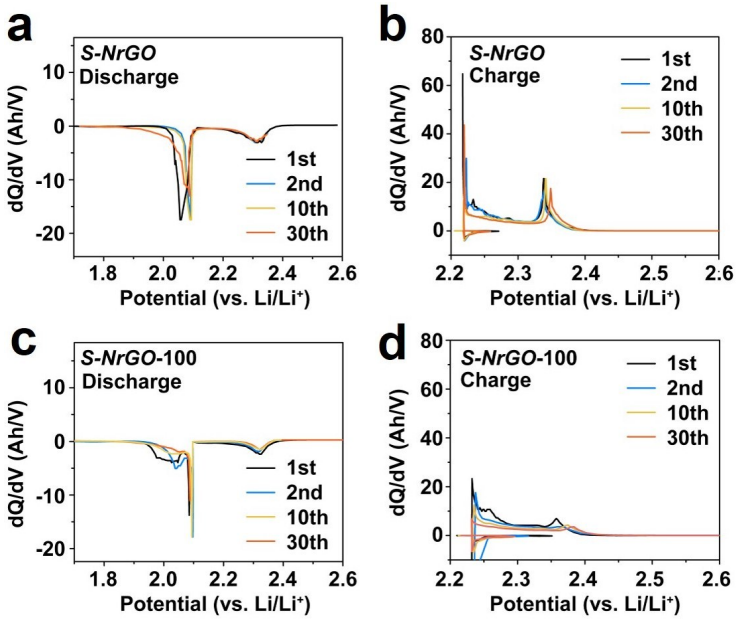

Fig. S12 Differential capacity plots. (a) Discharge and (b) charge process the S-*N*rGO at 0.1 C. (c) Discharge and (d) charge process the S-*N*rGO-100 electrodes at 0.1 C. The electrolyte was composed of 1 M LITFSI and 0.5 M $LiNO_3$ in DOL:DME (1:1, *v/v*). The sulfur mass loading of the electrodes is ~ 6.2 mgS/cm^2. The E/S ratio was 4.

As shown in the differential capacity plots (DCP) of the S-*N*rGO electrode (Fig. S12a and S12b) obtained from galvanostatic cycling test results (Fig. 4b), the S-*N*rGO electrode maintains the shape of the DCP peaks after the first discharge process. Due to the absence of lithium polysulfide in the electrolyte at the beginning of the cycling, some portion of the dissolved sulfur in the form of lithium polysulfides is not reduced at the sulfur electrode until the end of the discharge process which results in an initial capacity loss. Once lithium polysulfide is present in the electrolyte, the shape of the DCP peak is maintained, unless there are other factors strongly influencing the electrochemical process (e.g. reconfiguration of sulfur electrode causing an increase of the cell impedance, simultaneous loss of sulfur from the sulfur electrode due to the polysulfide shuttle effect) While the S-*N*rGO electrode maintains the shape of the DCP peaks for 30 cycles, the S-*N*rGO-100 electrode exhibited significant deformation and intensity decrease of the DCP peaks (Fig. S12c and 12d), indicating that continuous irreversible change occurs during cycling.

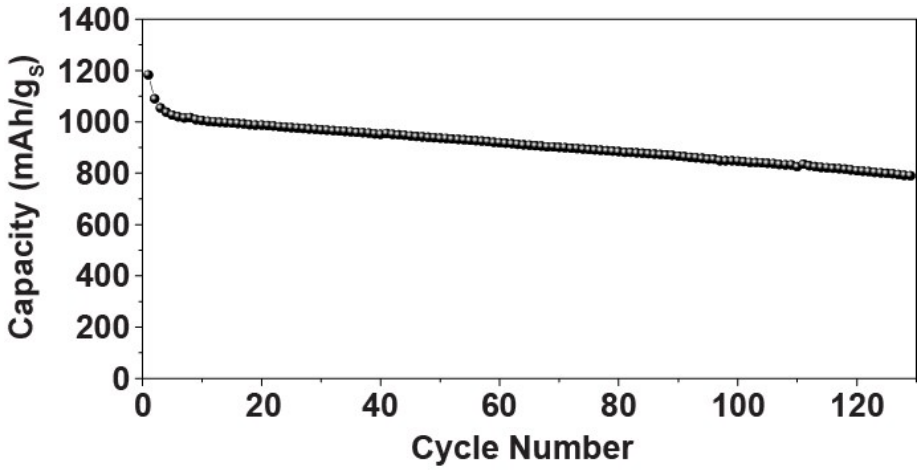

Fig. S13 Cycling performance of the S-*N*rGO electrode. The electrolyte was composed of 1.0 M LITFSI and 0.5 M $LiNO_3$ in DOL:DME (1:1, *v/v*). The sulfur mass loading of the electrodes was 3.0 mgS/cm^2. The E/S ratio was 5.

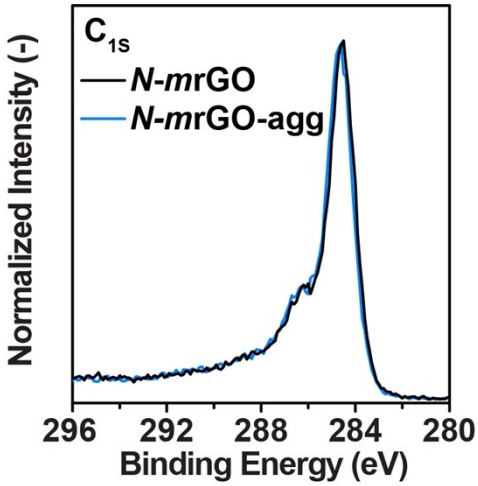

Fig. S14. XPS results of the *N*rGO and the aggregated *N*rGO composites.

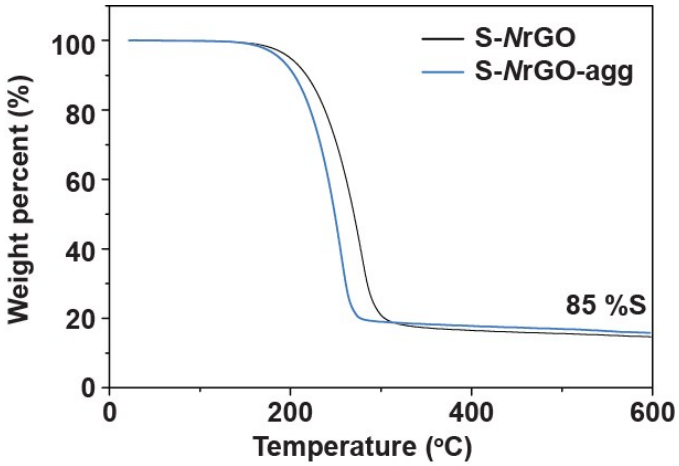

Fig. S15 TGA results of the S-*N*rGO and the aggregated S-*N*rGO composites under Ar atmosphere with a temperature ramping rate of 5.0 °C/min.

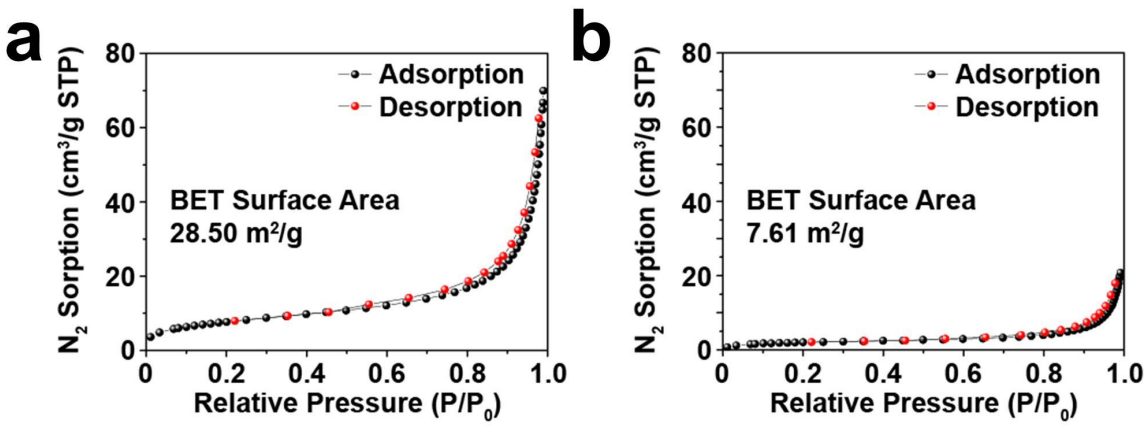

Fig. S16 BET surface area measurement results of (a) the S-*N*rGO and (b) the aggregated S-*N*rGO composites.

Both exhibit Type **2** behavior with no hysteresis that is a typical isotherm of macroporous structure, but the S-*N*rGO shows more high and clear B point at 0.1 of P/P_0 than the aggregated S-*N*rGO. The B point of the N_2 adsorption/desorption isotherm generally indicates complete monolayer coverage. This obvious B point of the S-*N*rGO combined with the HIM image supports a fact that our lyophilization process makes a reticulated porous structure, which promotes reversible transport of Li^+ within the sulfur electrode. On the other hand, an unclear B point is observed for the aggregated S-*N*rGO indicating that a common drying process using thermal treatment leads to a non-porous and closed structure.

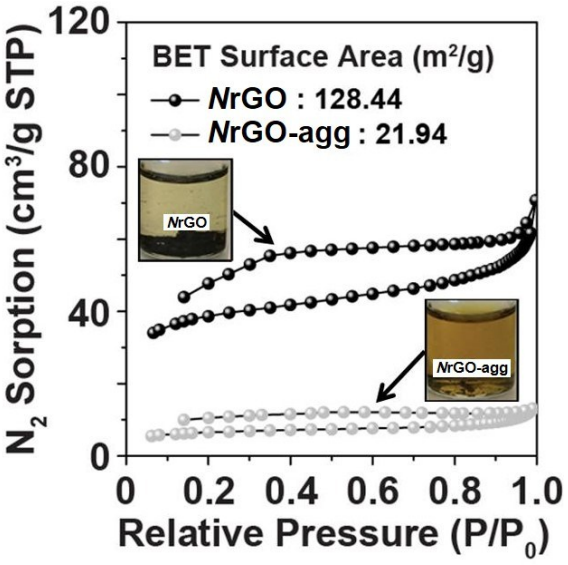

Fig. S17 BET surface area measurement results of the *N*rGO and the aggregated *N*rGO powders. (Inset photo: Polysulfide absorption test results of the *N*rGO and the aggregated *N*rGO powder)

For the polysulfide absorption test of the *N*rGO, 1 mg of the *N*rGO powder was put into a test solution composed of 0.008 M Li_2S_8 in 2 mL of DOL/DME mixture (1:1, *v/v*). The polysulfide test solution of the *N*rGO powder was almost colorless, which is indicative of the depletion of the polysulfides in the test solution, while the test solution color of the aggregated *N*rGO powder remained dark orange.

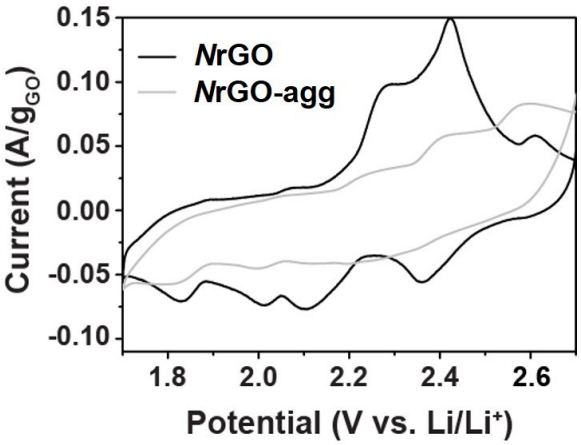

Fig. S18 Cyclic voltammetry test results of the *N*rGO and the aggregated *N*rGO electrodes at 0.1 mV/s. The electrolyte was composed of DOL:DME (1:1, *v/v*) with 1.0 M LITFSI and 0.008 M Li_2S_8.

Cyclic voltammetry (CV) results of the *N*rGO and the aggregated *N*rGO electrodes with a catholyte containing 0.008 M nominal Li_2S_8 are consistent with the chemical polysulfide adsorption tests, where the *N*rGO electrode exhibited distinct cathodic and anodic peaks during the discharge and charge processes, whereas the aggregated *N*rGO electrode showed cathodic and anodic peak shifts due to the larger overpotential of the aggregated *N*rGO electrode. Considering the fact that both the *N*rGO and the aggregated *N*rGO powder have the same chemical structure (Fig. S13), the results emphasize that the reticulated structure of the *N*rGO in the electrode is vital to fully utilize its effectiveness.

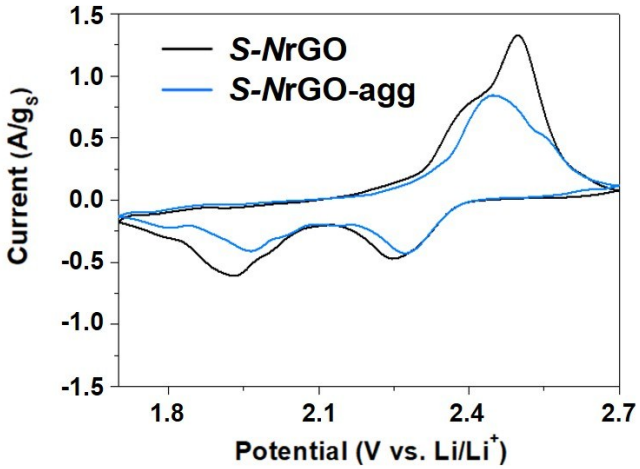

Fig. S19 Cyclic voltammetry test results of the S-*N*rGO and the aggregated S-*N*rGO electrodes at 0.1 mV/s. The electrolyte was composed of DOL:DME (1:1, *v/v*) with 1.0 M LITFSI and 0.5 M $LiNO_3$.

Cyclic voltammetry (CV) results of the S-*N*rGO and the aggregated S-*N*rGO electrodes are shown in Fig. S18. Both the S-*N*rGO and the aggregated S-*N*rGO electrodes exhibited distinct redox peaks during the cycling, however, the redox peaks of the S-*N*rGO electrode showed significantly sharper and larger specific current, indicating faster and more active electrochemical reaction of the S-*N*rGO than the aggregated S-*N*rGO electrode.

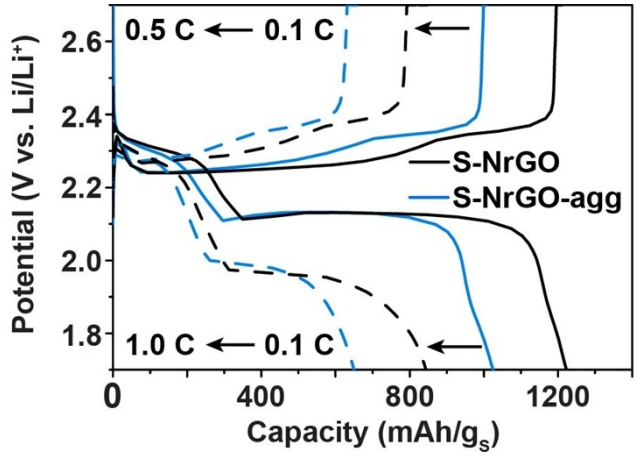

Fig. S20 Voltage profiles of the S-*N*rGO and the aggregated S-*N*rGO electrodes. Electrode loading was ~ 1.0 mgS/cm^2. Electrolyte was composed of $PYR_{14}TFSI$:DOL:DME (2:1:1, *v/v/v*) with 1.0 M LITFSI and 0.21 M $LiNO_3$.The cells were cycled at 0.1 C and 1.0 C for the first cycle and the following cycles, respectively.

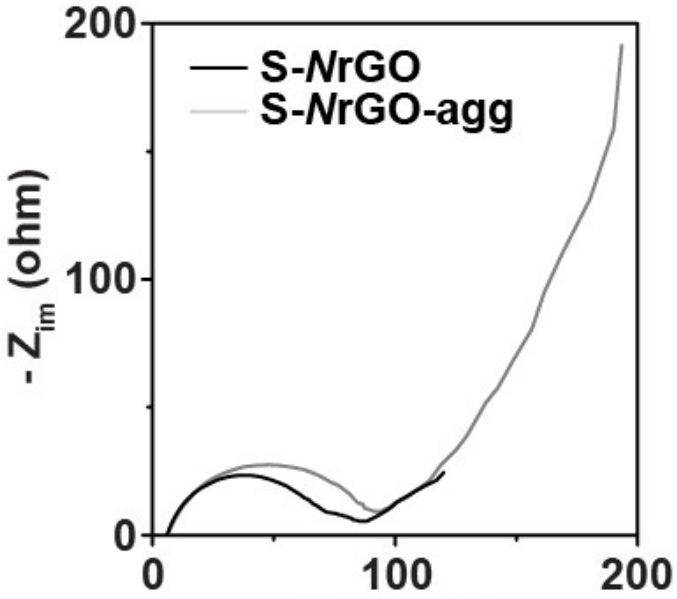

Fig. S21 Electrochemical impedance spectroscopy results of the S-*N*rGO and the aggregated S-*N*rGO electrodes. Nyquist plots obtained in the frequency range of 10.0 mHz to 1.0 MHz. Electrode loading was ~ 1.0 mgS/cm^2. Electrolyte was composed of $PYR_{14}TFSI$:DOL:DME (2:1:1, *v/v/v*) with 1.0 M LITFSI and 0.21 M $LiNO_3$.

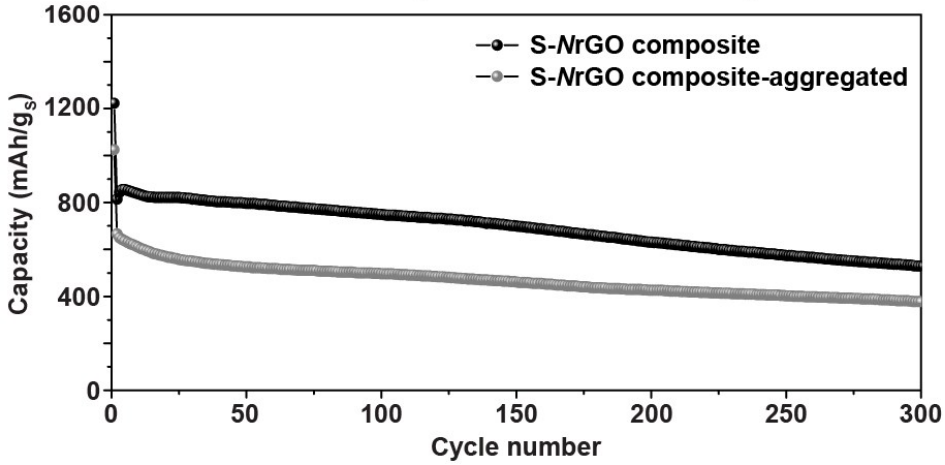

Fig. S22 Galvanostatic cycling test results of the S-*N*rGO and the aggregated S-*N*rGO electrodes. Electrode loading was ~ 1.0 mgS/cm^2. Electrolyte was composed of $PYR_{14}TFSI$:DOL:DME (2:1:1, *v/v/v*) with 1.0 M LITFSI and 0.21 M $LiNO_3$.The cells were cycled at 0.1 C and 1.0 C for the first cycle and the following cycles, respectively.

Table S1 Current state-of-the-art of sulfur electrodes (> 3 mgS/cm^2) with a conventional aluminum foil current collector that were cycled at least 25 cycles.

Ref.	S loading (mg/cm^2)	S Content[a] (wt.%)	E/S ratio (μl/mgS)	Peak capacity (mAh/gS)	Current	Energy[b] (Wh/kg)
This Work	6.2	63.0	4.0	1180.0	0.3 mA/cm^2	324.6
#1	4.0	70.0	5.0	1300.0	0.2 mA/cm^2	289.8
#2	6.7	76.0	5.0	1120.0	0.67 mA/cm^2	286.3
#3*	3.0	69.8	7.0	1419.0	C/20	242.6
#4	5.5	72.0	7.0	~1200.0	0.65 mA/cm^2	237.9
#5	4.0	64.0	5.0	860.0	C/10	189.1
#6*	10.0	42.2	13.0	1332.0	C/10	169.3
#7*	13.9	55.0	15.0	1383.0	C/20	164.7
#8	4.0	60.0	15	1400.0	C/50	151.4
#9	4.0	56.8	15.0	1200.0	C/5	129.2
#10	3.2	64.0	12.5	1017.0	C/10	121.7
#11	4.6	60.0	15	1097.0	C/5	120.8
#12*	3.0	52.0	30.0	1000.0	0.6 mA/cm^2	59.6
#13*	3.37	62.1	40	860.0	C/5	40.7
#14*	4.5	<80.0	<33.3	621.0	C/5	35.6
#15	4.7	80.0	Unknown	~1250.0	C/20	N/A
#16	4.2	70.0	Unknown	1100.0	0.35 mA/cm^2	N/A
#17*	3.5	<48.2	Unknown	~1400.0	C/5	N/A
#18	3.5	49.7	Unknown	1147.0	C/5	N/A
#19	3.0	72.0	Unknown	860.0	C/10	N/A
#20	3.95	64.3	Unknown	956.0	C/5	N/A
#21*	3.0	54.5	Unknown	1290.0	C/5	N/A
#22	3.0	80.0	Unknown	1123.0	C/10	N/A

a: S content calculation includes the weight of the interlayer

b: Specific energy estimated with consideration of following parameters: S loading; S content; Electrolyte weight (assumption: density of electrolyte as 1); Peak capacity; working potential (2.15 V); Aluminum foil weight (6.0 mg/cm^2); Copper foil weight (4.0 mg/cm^2); Li metal weight (mole ratio between sulfur and lithium=1:2); Separator weight (1.13 mg/cm^2).

*: The cell includes an interlayer(s) or a specially-coated separator)

Table S2 Content of carbon, nitrogen and oxygen in the prepared *N*rGO and the *N*rGO-100 samples demonstrated by elemental analysis.

Element	Carbon	Nitrogen	Oxygen
*N*rGO	77.94	5.04	17.02
*N*rGO-100	80.55	6.33	13.12

Supporting References for Experimental Section

1. H. W. Kim, M. B. Ross, N. Kornienko, L. Zhang, J. Guo, P. Yang & B. D. McCloskey Nat. Catal. 2018, **1**, 282.

Supporting References for Supplementary Figures

1. A. Kawase and E. J. Cairns, *J. Electrochem. Soc*, 2018, **165**, A3257-A3262.

Supporting References for Table S1

1. S. Chen, Y. Gao, Z. Yu, M. L. Gordin, J. Song and D. Wang, *Nano Energy*, 2017, **31**, 418.
2. F. Zeng, A. Wang, W. Wang, Z. Jin and Y.-S. Yang, *J. Mater. Chem. A*, 2017, **5**, 12879.
3. F. Zeng, Z. Jin, K. Yuan, S. Liu, X. Cheng, A. Wang, W. Wang and Y.-S. Yang, *J. Mater. Chem. A*, 2016, 4, 12319.
4. F. Zeng, W. Wang, A. Wang, K. Yuan, Z. Jin and Y.-S. Yang, *ACS Appl. Mater. Int.*, 2015, **7**, 26257.
5. H. Pan, K. S. Han, M. H. Engelhard, R. Cao, J. Chen, J.-G. Zhang, K. T. Mueller, Y. Shao and J. Liu, Adv. Funct. Mater, 2018, **28**, 1707234.
6. H. M. Kim, H.-H. Sun, I. Belharouak, A. Manthiram and Y.-K. Sun, ACS Energy Lett. 2016, 1, 136-141.
7. L. Qie and A. Manthiram, ACS Energy Lett. 2016, 1, 46-51.
8. A. Schneider, C. Weidmann, C. Suchomski, H. Sommer, J. Janek and T. Brezesinski, Chem. Mater. 2015, 27, 1674-1683.
9. Y. Mi, W. Liu, J. Jiang, G. W. Brudvig, H. Zhou and H. A. Wang, J. Mater. Chem. A 2017, 5, 11788-11793.
10. T. Chen, B. Cheng, G. Zhu, R. Chen, Y. Hu, L. Ma, H. Lv., Y. Wang, J. Liang, Z. Tie, Z. Jin and Z. Liu, Nano Lett. 2017, 17, 437-444.
11. L. J. Seop, J. Jaemoon, J. Jyongsik and A. Manthiram, Small 2017, 13, 1602984.
12. Z. Liu, B. Liu, P. Guo, X. Shang, M. Lv, D. Liu and D. He, Electrochim. Acta 2018, 269, 180-187.
13. J. Zhu, Y. Ge, D. Kim, Y. Lu, C. Chen, M. Jiang and X. Zhang, Nano Energy 2016, 20, 176-184.
14. S. Waluś, A. Robba, R. Bouchet, C. Barchasz and F. Alloin, Electrochim. Acta 2016, 210, 492-501.
15. D. Lv, J. Zheng, Q. Li, X. Xie, S. Ferrara, Z. Nie, L. B. Mehdi, N. D. Browning, J. Zhang, G. L. Graff and J. Xiao, Adv. Energy Mater. 2015, 5, 1402290.
16. J. Song., T. Xu, M. L. Gordin, P. Zhu, D. Lv, Y.-B. Jiang, Y. Chen, Y. Duan and D. Wang, Adv. Funct. Mater. 2014, 24, 1243-1250.

17. J. Balach, T. Jaumann, M. Klose, S. Oswald, J. Eckert and L. Giebeler, Adv. Funct. Mater. 2015, 25, 5285-5291.
18. Z. Li, J. Zhang and X. W. Lou, Angew. Chem. Int. Ed. 2015, 54, 12886-12890.
19. S. Liu, Y. Li, X. Hong, J. Xu, Z. Chunman and K. Xie, Electrochim. Acta 2016, 188, 516-522.
20. J. Balach, T. Jaumann, M. Klose, S. Oswald, J. Eckert and L. Giebeler, J. Power Sources 2016, 303, 317-324.
21. G. Ma, Z. Wen, Q. Wang, C. Shen, P. Peng, J. Jin and X. Wu, J. Power Sources 2015, 273, 511-516.
22. G. Ai, Y. Dai, W. Mao, H. Zhao, Y. Fu, X. Song, Y. En, V. S. Battaglia, V. Srinivasan and G, Liu, Nano Lett. 2016, 16, 5365-5372.